Chinese Chemical Letters 34 (2023) 107812

Contents lists available at ScienceDirect

Chinese Chemical Letters

journal homepage: www.elsevier.com/locate/cclet

Single-atom rhodium anchored on S-doped black phosphorene as a promising bifunctional electrocatalyst for overall water splitting

Xinyi Li[a], Zhongxu Wang[a], Yu Tian[b], Xiaofeng Li[a,*], Qinghai Cai[a,c], Jingxiang Zhao[a,*]

[a] *College of Chemistry and Chemical Engineering, and Key Laboratory of Photonic and Electronic Bandgap Materials, Ministry of Education, Harbin Normal University, Harbin 150025, China*
[b] *Institute for Interdisciplinary Quantum Information Technology, Jilin Engineering Normal University, Changchun 130052, China*
[c] *Heilongjiang Province Collaborative Innovation Center of Cold Region Ecological Safety, Harbin 150025, China*

ARTICLE INFO

Article history:
Received 7 August 2022
Revised 4 September 2022
Accepted 6 September 2022
Available online 11 September 2022

Keywords:
Overall water splitting
Bifunctional catalysts
Single-atom catalysts
S-doped black phosphorene
Density functional theory computations

ABSTRACT

Superior bifunctional electrocatalysts with ultra-high stability and excellent efficiency are crucial to boost the oxygen evolution reaction (OER) and the hydrogen evolution reduction (HER) in the overall water splitting (OWS) for the sustainable production of clean fuels. Herein, comprehensive density functional theory (DFT) computations were performed to explore the potential of several single transition metal (TM) atoms anchored on various S-doped black phosphorenes (TM/S_{nx}-BP) for bifunctional OWS electrocatalysis. The results revealed that these candidates display good stability, excellent electrical conductivity, and diverse spin moments. Furthermore, the Rh/S_{12}-BP catalyst was identified as an eligible bifunctional catalyst for OWS process due to the low overpotentials for OER (0.43 V) and HER (0.02 V), in which Rh and its adjacent P atoms were identified as the active sites. Based on the computed Gibbs free energies of OH*, O*, OOH* and H*, the corresponding volcano plots for OER and HER were established. Interestingly, the spin moments and the charge distribution of the active sites determine the catalytic trends of OER and HER. Our findings not only propose a promising bifunctional catalyst for OWS, but also widen the potential application of BP in electrocatalysis.

In the last decades, the exhaustion of conventional fossil fuels and the detrimental environmental issues has inspired the global investigation to develop alternative clean and renewable energy technologies [1–4]. Thanks to its high energy density and zero carbon emission, hydrogen energy has been widely considered as an excellent alternative to traditional fossil fuels [5–7]. Among various hydrogen production devices, electrochemical overall water splitting (OWS) has attracted increasing interest as a promising technology for generating hydrogen by renewable energy under mild conditions [8–11]. Notably, the hydrogen evolution reaction (HER) and the oxygen evolution reaction (OER) are two key half reactions to greatly affect the performance for the large-scale commercial applications of OWS due to their sluggish kinetics and low efficiency [12,13]. At present, Pt and Ru/Ir-based materials represent the most advanced catalysts for HER and OER, respectively. Unfortunately, the high cost and scarcity of these noble metals largely hinder their widespread usage [14–17]. In addition, the combination of two different electrocatalysts into one integrated electrolyzer could complicate the procedure and induce the unsatisfied OWS performances due to the mismatch of the electrolyte pH. Thus, it is of significant importance to downsize the noble-metal catalysts to single-atom catalysts (SACs) or effectively substitute the noble-metal catalysts with non-noble-metal catalysts for HER and OER that can work in the same electrolyze for the commercial OWS [18].

Recently, SACs have been widely used in electrocatalytic water splitting reactions due to their high activity and selectivity [19–21]. Notably, SACs are generally anchored within porous and conductive support to ensure its high stability. In this respect, the 2D materials have been widely regarded as ideal support substrates to stabilize the SACs due to the great surface area, superior carrier mobility, and excellent thermal durability [22–24]. Black phosphorous (BP), as the most stable allotrope of the element phosphorus with a two-dimensional (2D) layered structure, has been triggering extensive interest due to its unique structural and excellent properties, such as tunable band gap and high carrier mobility, endowing it wide applications in transistors, supercapacitors, catalysis, batteries and sensors [25–28]. Among these applications, BP-based electrocatalysts are of our particular interest. For example, Zhang and co-workers reported the excellent electrocatalytic OER activ-

---

[*] Corresponding authors.
E-mail addresses: lixiaofeng@hrbnu.edu.cn (X. Li), zhaojingxiang@hrbnu.edu.cn (J. Zhao).

https://doi.org/10.1016/j.cclet.2022.107812

ity of few-layer BP nanosheets [29], while Wang's group showed that the well-exfoliated BP nanosheets can perform as an efficient catalyst for electrochemical nitrogen reduction reaction (NRR) [30]. Although some studies revealed that BP sheets exhibit good electrocatalytic activities for OER, the HER electrocatalytic activity is poor, as the densely packed lone-pair p electrons of the P atoms make them difficult to adsorb hydrogen species [31]. In addition, the instability of BP in water and oxygen environment is also an obstacle for achieving highly efficient HER/OER catalytic performances [32,33]. Thus, how to effectively improve the stability and the HER/OER catalytic activity of BP nanosheet still remains a huge challenge.

To this end, some interesting strategies have been proposed, including encapsulation and chemical modification to enhance the stability of BP nanosheet in the illumination, oxygen, and water environment [34,35]. Especially, the introduction of nonmetal heteroatoms of was recently regarded as an effective way not only to avoid the degradation of BP in the air moisture environment, but also to modulate its electronic and magnetic properties for wide applications [36]. For example, Lv *et al.* fabricated a feasible approach to hamper the degradation of BP by sulfur (S) doping, which can be utilized as field-effect transistors [37], while Xu *et al.* demonstrated that their prepared N-doped BP exhibits high electrocatalytic activity towards NRR [38]. On the other hand, metal incorporation can also maintain the structural integrity of BP by tuning its band gap. For example, Li *et al.* showed the high efficiency of the PtRu nanoclusters decorated BP in HER [39], while Qiao and Shi independently found that the synthesized Au and Co nanoparticles on BP exhibit excellent OER catalytic activity [40,41].

Inspired by these pioneering reports, here, we performed comprehensive density functional theory (DFT) computations to study the electrocatalytic activity of several single transition metal (TM) atoms anchored on different S-doped BP monolayers (TM represent Mn, Fe, Co, Ni, Cu, Rh, Ru, Pd and Ir, which have been widely reported as the common HER/OER electrocatalysts). Our results demonstrated that most of TM atoms anchored on BP-based substrates exhibit outstanding stability, reduced band gap, and excellent magnetic properties. Interestingly, the Rh/S_{12}-BP was revealed as a bifunctional electrocatalyst with high-efficiency with low overpotential (0.43/0.02 V for OER/HER), in which the Rh atom and its adjacent P atom perform as the active sites. Remarkably, the high OER activity of Rh/S_{12}-BP can be ascribed to its optimal magnetic moment, whereas the moderate charge of the P site boost its superior HER performance. Our work not only offers an effective strategy to construct high-efficient bifunctional catalyst for overall water splitting, but also further widens the application of BP for energy storage.

Every spin-polarized computation was performed using the DFT method, as achieved in the Vienna Ab initio Simulation Package (VASP) [42]. The projector augmented wave (PAW) means was used to treat the interaction of ions with electrons [43,44]. The exchange-correlation interaction was explained by the generalized gradient approximation (GGA) with the Perdew–Burke–Ernzerhof (PBE) functional [45,46]. The dispersion corrections (DFT+D3) in Grimme scheme was employed to describe the long-range van der Waals (vdW) effects [30]. A cutoff energy of 500 eV was used for the plane-wave basis set, and the convergence criteria for force and energy during geometrical optimization were set to 0.01 eV/Å and 10^{-5} eV, respectively. An implicit solvent model VASPsol was adopted to treat the solvation effect with the dielectric constant of 78.4 for water. Bader charge analysis was utilized to compute the involved charge transfer [47].

A (4×4) supercell with a monovacancy was built to simulate the behavior of BP, which contains 63 atoms with a vacuum gap of 20 Å. A Monkhorst-Pack mesh with $5 \times 5 \times 1$ *K*-points was employed for Brillouin zone integration. *Ab initio* molecular dynamics simulations (AIMD) were carried out to assess the thermal stabilities of TM atoms on the BP-based substrate in a canonical ensemble (NVT), in which the time step was set as 1.0 fs for a total simulation time of 10 ps.

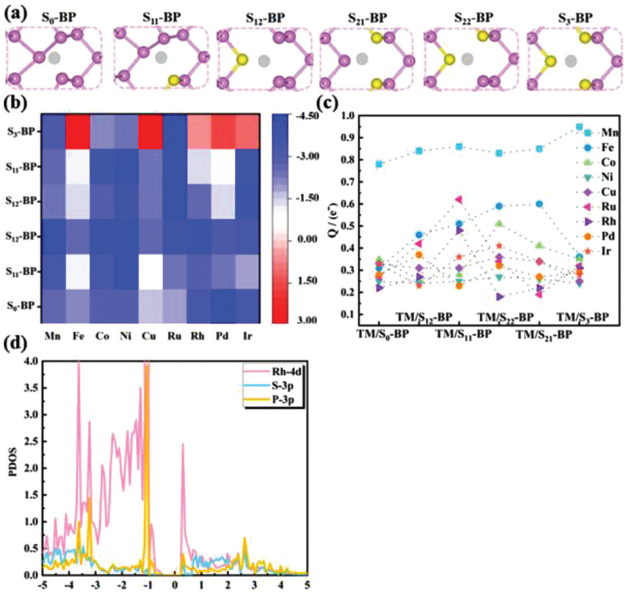

Fig. 1. (a) The structures of six BP based substrates. (b) Top and side views of the TM/S_{nx}-BP catalysts. The blue balls represent the loaded transition–metal atoms. The yellow balls denote the doped sulfur atoms, and the pink balls are phosphorus atoms. (b) The E_b values of TM/S_{nx}-BP candidates. (c) The Bader charge analysis of TM/S_{nx}-BP candidates. (d) The computed partial density of states (PDOSs) of Rh/S_{12}-BP catalyst.

The formation energy (E_f) of S dopants in BP was determined by: $E_f = E_{S_x-BP} - E_{S_0-BP} - x\mu_S + x\mu_P$, where, E_{S_x-BP} and E_{S_0-BP} are the total energies of S_x–BP ($x = 1-3$) and S_0–BP without S dopant, respectively, and x is the number of introduced S atoms. μ_S and μ_P are the chemical potentials of S and P, respectively. μ_S was computed according to the S_8 material and μ_P referred to the bulk phase of BP. The free energy change (ΔG) of each elementary step in HER/OER was obtained according to the computational hydrogen electrode (CHE) suggested by Nørskov *et al.* and more computation details were presented in the Electronic Supporting Information (ESI).

Previous scientific research revealed that the geometric and electronic structures of single metal atom catalysts significantly depend on their coordinating microenvironment, which in turn determines their performances in catalytic processes [48–53]. To this end, different numbers of S dopants were introduced into different sites of BP monolayer, which were labeled as S_{nx}-BP, where n and x represent the numbers ($n = 0$, 1, 2 and 3) and sites (upper and sublayer) of the introduced S dopants, respectively. As a result, six BP-based substrates were obtained as shown in Fig. 1a. Remarkably, relative to the un-doped S_0-BP system, the formation energies of these S-doped BP monolayers are computed to be 0.68, 0.67, 0.95, 1.04 and 1.40 eV, respectively, suggesting that S-doped BP is more difficult to be synthesized when more S dopants were introduced. Then, nine single Mn, Fe, Co, Ni, Cu, Rh, Ru, Pd and Ir atoms were anchored on the vacancy of the six S-doped BP substrates, thus generating 54 TM/S_{nx}-BP structures as the potential catalysts of HER and OER.

After fully geometrical optimization, we found that all TM/S_{nx}-BP systems possess similar configurations, namely, these single TM atoms can be firmly embedded into the vacancy of these S-doped BP substrates (Fig. S1 in Supporting information), leading to the formation of TM-S and TM-P bonds with the length of 2.13 Å to

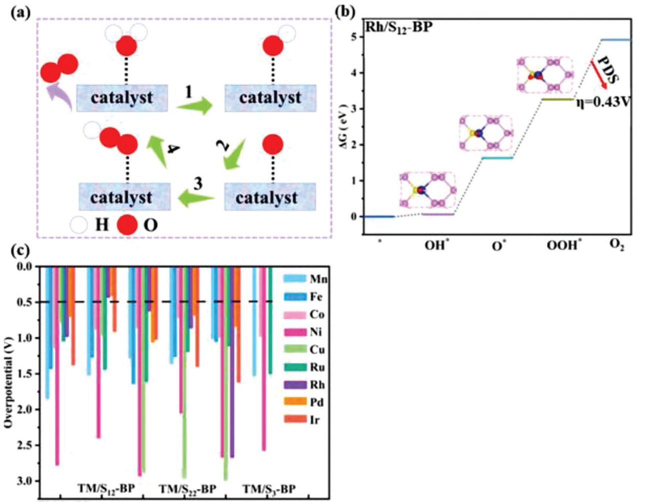

Fig. 2. (a) The schematics of the 4e process of the OER occurring on TM/S$_{nx}$-BP systems. (b) Free-energy diagrams for OER on Rh/S$_{12}$-BP monolayer. (c) The η^{OER} values on all TM/S$_{nx}$-BP candidates.

2.52 Å. To ensure the practical applications of TM/S$_{nx}$-BP materials, the strong binding strength between single TM atoms and BP-based substrates is essential to prevent their agglomeration. To this end, the stabilities of TM/S$_{nx}$-BP systems were evaluated by computing their binding energies (E_b) according to the following equation: $E_b = E_{\text{TM/S-BP}}$ - $E_{\text{S-BP}}$ - E_{TM}, where $E_{\text{TM/S-BP}}$, $E_{\text{S-BP}}$ and E_{TM} represent the total electronic energies of TM/S$_{nx}$-BP, S$_{nx}$-BP, and single TM atom in the corresponding bulk materials, respectively. Based on this definition, a negative E_b value suggests that this TM atom can be stably adsorbed on BP substrates, rather than aggregating into larger metal cluster. We can clearly find out from Fig. 1b that most of TM/S$_{nx}$-BP candidates exhibit negative E_b values, indicating their high thermodynamic stability. Several exceptions are the anchoring of Fe, Co, Rh, Pd, and Ir on S$_3$-doped BP with positive ΔE_b values, suggesting their feasibility to form larger metal clusters, which are thus ruled out as promising HER and OER catalysts in the following discussion.

Based on the optimized TM/S$_{nx}$-BP configurations, we explored their electronic and magnetic properties. The Bader charge analysis showed that significant charge ($0.18e^- - 0.95e^-$) are transferred from TM atoms to BP-based substrates, making the anchored TM atoms carry considerable positive charge (Fig. 1c), which may perform as the active sites to capture the oxygenated species in OER. Furthermore, the computed partial density of states (PDOSs, Fig. 1d) suggested the strong hybridization of TM-*d* orbital with the 3*p* orbitals of S and P (P$_{21}$) atoms, in which Rh/S$_{12}$-BP was taken as an example (this material will be revealed to exhibit superior HER/OER catalytic activity later), again verifying the strong capability of S-doped BP substrates to immobilize single TM atoms. Excellent electrical conductivity is vital to ensure the rapid charge transfer for efficient HER and OER. Thus, the band structure of Rh/S$_{12}$-BP was computed to estimate its electrical conductivity. Remarkably, the results showed that Rh/S$_{12}$-BP possesses the semiconducting feature with a small band gap of 0.12 eV (Fig. S2 in Supporting information), suggesting its good electrical conductivity and thus facilitating its practical application in electrocatalysis.

Spin moment has been proved to be essential for designing efficient OER catalysts. For example, Li *et al.* reported that the single Co atom catalysts on TaS$_2$ monolayer exhibit superior OER performance due to its optimal spin density [54]. Interestingly, all considered TM/S$_{nx}$-BP systems exhibit remarkable spin moments with ranging from 0.08 μ_B to 3.78 μ_B, which are mainly centralized on the anchored TM atoms (Fig. S3 in Supporting information). Thus, the TM/S$_{nx}$-BP systems may exhibit high OER activity by carefully tuning the spin density of the anchored TM atoms.

To systematically explore the OER catalytic activity of these TM/S$_{nx}$-BP materials, the adsorbed oxygenated intermediates (*OH, *O and *OOH) during OER were fully optimized to then compute their adsorption free energies (ΔG_{OH^*}, ΔG_{O^*} and ΔG_{OOH^*}, Table S1 in Supporting information) [55]. Indeed, we found that these oxygenated intermediates are preferable to be adsorbed on the top of the positively charged TM atoms. To figure out the limiting-determining step, the Gibbs free energy differences of each elementary reaction step during OER (Fig. 2a) on these TM/S$_{nx}$-BP systems were computed, including (1) H_2O (l) decomposes to H^+ and *OH; (2) *OH dissociates to H^+ and *O; (3) *O reacts with the second H_2O to form *OOH; (4) O_2 (g) is released.

Again taking Rh/S$_{12}$-BP as an example, we can see from Fig. 2b that every elementary reaction step during the OER are uphill in the free energy profile with the ΔG values of 0.07, 1.56, 1.63 and 1.67 eV, respectively. Ideally, the free energy changes for all steps in OER are 1.23 eV to guarantee that the ΔG of each elementary step is zero at equilibrium potential (1.23 V), otherwise the adverse overpotential will be generated. Accordingly, the elementary step with the maximum free energy change ($\Delta G_{\max}$) is regarded as the limiting-determining step (PDS), which determines the overpotential of OER (η^{OER}):$\eta^{\text{OER}} = (\Delta G_{\max}$ – 1.23)/e. For Rh/S$_{12}$-BP, some elementary steps are still uphill at 1.23 V, indicating the existence of overpotential. Especially, the fourth step of O_2 desorption can be identified as the PDS due to its maximum ΔG value (1.67 eV) among all elementary steps, corresponding to the η^{OER} of 0.44 V. On the other hand, the η^{OER} values on other TM/S$_{nx}$-BP candidates were summarized in Fig. 2c, among which Pd/S$_{12}$-BP is shown to possess a low η^{OER} value of 0.41 V, and the PDS locates at the formation of *OOH species. Interestingly, the η^{OER} values of Rh/S$_{12}$-BP and Pd/S$_{12}$-BP are even lower than those of most advanced RuO_2/IrO_2 materials (about 0.50 V), indicative of their high catalytic efficiency for OER [56].

To gain further insight into the remarkable difference in OER electrocatalytic performance of these TM/S$_{nx}$-BP candidates, we constructed the relationships between Gibbs free energies of the adsorbed oxygenated intermediates ($\Delta G_{*\text{O}}$, $\Delta G_{*\text{OH}}$ and $\Delta G_{*\text{OOH}}$) to find a descriptor to elucidate OER catalytic trend [57–59]. According to the computed $\Delta G_{*\text{O}}$, $\Delta G_{*\text{OH}}$ and $\Delta G_{*\text{OOH}}$ values, we found that $\Delta G_{*\text{OOH}}$ can be written as a function of ΔG_{OH^*} by: $\Delta G_{*\text{OOH}} = 0.90\Delta G_{*\text{OH}} - 3.32$ eV with the coefficient of determination of 0.94 (Fig. 3a), indicating a strong linear relationship between each other, which is well consistent with the previous theoretical reports on carbon-based catalysts for OER. Based on the obtained scaling relations, the volcano plot was determined by choosing $\Delta G_{*\text{O}} - \Delta G_{*\text{OH}}$ as a descriptor for OER activity (Fig. 3b), in which Rh/S$_{12}$-BP and Pd/S$_{12}$-BP are standing near the peak of OER volcano plots, proving their excellent OER catalytic activities.

Furthermore, we established a contour map of OER activity on TM/S$_{nx}$-BP catalysts by choosing $\Delta G_{*\text{OH}}$ and $\Delta G_{*\text{O}} - \Delta G_{*\text{OH}}$ as the descriptors (Fig. 3c), which has been broadly used to explain the OER catalytic trends. Notably, the whole contour map was divided into four regions, corresponding to the ΔG values of four elementary steps during OER. For some TM/S$_{nx}$-BP with smaller $\Delta G_{\text{O}^*} - \Delta G_{\text{OH}^*}$ than 1.50 eV, OER process is dominated by the third step of $\text{O}^* \rightarrow \text{OOH}^*$. With the $\Delta G_{*\text{O}} - \Delta G_{*\text{OH}}$ values gradually increasing, the formation of *O from *OH becomes the PDS. Among all considered catalysts, only Rh/S$_{12}$-BP and Pd/S$_{12}$-BP locate at the optimal position and show low overpotentials (0.44 and 0.41 V), corresponding to the $\Delta G_{*\text{O}} - \Delta G_{*\text{OH}}$ of 1.50 eV and thus demonstrating their superior OER catalytic performance.

In order to shed in-deep light on the origin of the electrocatalytic performance of these TM/S$_{nx}$-BP catalysts, the variation of

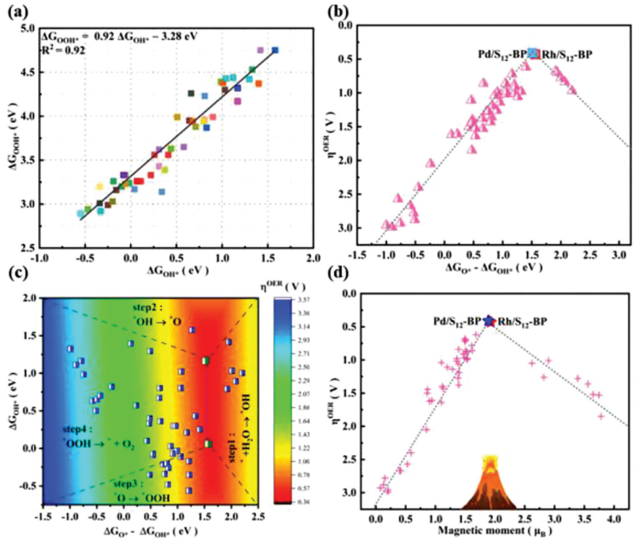

Fig. 3. (a) Scaling relationships for Gibbs adsorption free energy of OOH* *vs.* OH*. (b) Relationship between OER overpotential (η) and $\Delta G_{*O} - \Delta G_{*OH}$ values. (c) Relationship between OER overpotential (η) and two independent descriptors $\Delta G_{O^*} - \Delta G_{OH^*}$ and ΔG_{OH^*}. (d) Scaling relationship of OER overpotential (η) *versus* (μ_B) on TM/S$_{nx}$-BP catalysts.

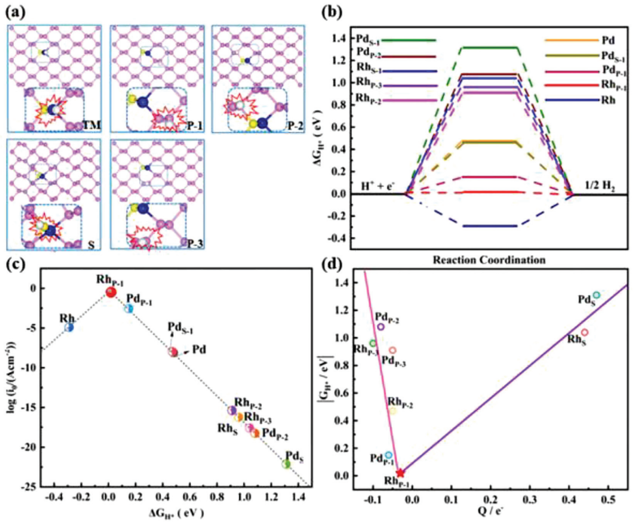

Fig. 4. (a) Constructed models for the adsorption of H atomic sites. (b) The computed free energy profiles for the HER (c) The obtained volcano curve of the exchange current i_0 *versus* the Gibbs free energy of hydrogen adsorption ΔG_{H^*} values on various catalysts. (d) Scaling relationship of $|\Delta G_{H^*}|$ *versus* (Q) on TM/S$_{nx}$-BP monolayers.

their η^{OER} values with the spin moments of the TM active sites was also plotted (Fig. 3d). Interestingly, an obvious volcano is obtained, revealing the spin density dependent OER activity. Clearly, either too small or too large spin moments will lead to an unsatisfied OER catalytic activity, whereas the optimal spin densities on Rh/S$_{12}$-BP and Pd/S$_{12}$-BP well account for their superior OER performance, which again locate at the peak of the volcano plot. Thus, the spin density in SACs may be utilized as an ideal descriptor to rapidly screen out the efficient magnetic SACs for OER, well consistent with previous reports [60].

Then, the HER catalytic performances of TM/S$_{nx}$-BP with good OER activities (Rh/S$_{12}$-BP and Pd/S$_{12}$-BP with $\eta^{OER} \leq 0.50$ V of RuO$_2$/IrO$_2$) were explored by computing the Gibbs free energy of the adsorbed hydrogen (ΔG_{H^*}), which has been widely regarded as a critical descriptor to assess the HER activity of a given material. Ideally, the ΔG_{H^*} value of an eligible HER electrocatalyst should be close to 0 eV [61–63]. In contrast, too positive or too negative ΔG_{H^*} values indicate too weak or too strong H* adsorption on the catalysts, thus hindering the HER activity.

Consistent with previous studies, we found that the ΔG_{H^*} value on the pristine BP is as high as 1.29 eV [64], indicating that H* adsorption is rather weak and pristine BP is not good for HER. As for H* adsorption on Rh/S$_{12}$-BP and Pd/S$_{12}$-BP, both Rh or Pd and their adjacent P and S sites were considered as the active sites (Fig. 4a). The results displayed that the ΔG_{H^*} values on most of active sites, such as Pd, P$_2$, P$_3$ and S sites are highly positive (0.40~1.38 eV), suggesting a poor HER activity. In contrast, the Rh site exhibits a strong reactivity towards H* species with a more negative ΔG_{H^*} value (−0.29 eV), thus ruling out as HER activity site due to the too strong adsorption. Interestingly, the ΔG_{H^*} values on the P$_1$ sites of Rh/S$_{12}$-BP and Pd/S$_{12}$-BP are calculated to be 0.02 and 0.15 eV (Fig. 4b), respectively, indicating that the two sites can perform as active sites for efficient HER, especially for Rh/S$_{12}$-BP.

To clearly observe the remarkable difference in the HER catalytic activity on the different sites of Rh/S$_{12}$-BP and Pd/S$_{12}$-BP catalysts, a volcano curve was plotted using exchange current (i_0, ESI) as a function of the ΔG_{H^*} [65,66]. According to the well-established Sabatier's principle, both too strong (such as Rh site) and too weak (such as S site) H* adsorption will result in a low exchange current. Interestingly, the P$_1$ site of Rh/S$_{12}$-BP with ΔG_{H^*} (0.02 eV) close to zero achieves the maximum exchange current rate, and it thus locates the peak of the volcano (Fig. 4c).

This superior catalytic performance of P$_1$ site could be attributed to the charge redistribution after single Rh and Pd atoms were anchored. In detailed, the P$_1$, P$_2$ and P$_3$ atoms carry about 0.04 |e$^-$| negative, while significant positive charges (about 0.45 |e$^-$|) locate on the connected S atoms. Interestingly, the HER catalytic activity can be highly correlated the charge distribution of these active sites. As shown in Fig. 4d, an inversed volcano plot is obtained, in which the P$_1$ site of Rh/S$_{12}$-BP system is situating near the peak (Fig. 4d), agreeing with its excellent HER performance due to its optimal H* binding strength. For the practical applications of Rh/S$_{12}$−BP as electrocatalysts, in addition to the high activity reflected by low overpotential, its electrochemical stability in aqueous solution is also of our concern, which is important to know whether the bare surfaces of Rh/S$_{12}$-BP could be covered by *O/*OH species under working conditions [67]. To address this question, we constructed the surface Pourbaix diagram of Rh/S$_{12}$-BP to reveal the most stable surface configurations at different equilibrium potentials and pH values (ESI). Based on the obtained oxidation potentials and the limiting potentials at pH 0, we found that the limiting potential (−1.67 V) of OER on Rh/S$_{12}$-BP catalyst is much lower than the oxidation potentials (0.07, 1.57 and 1.63 V) of different oxidation species (Fig. S4a in Supporting information). Thus, we predicted that the oxidation of single Rh atom catalyst anchored on this S-doped BP substrate during OER process will be greatly suppressed, suggesting that its outstanding stability against the electrolyte solvent at the realistic electrochemical operations.

In addition, we computed the dissolution potential (U_{diss}, computational details are shown in Supporting information) of Rh in the Rh/S$_{12}$−BP catalyst at pH 0 (U_{diss} values of other catalysts are in Table S1 in Supporting information), where a positive U_{diss} value suggest a good electrochemical stability [68]. Interestingly, the computed U_{diss} value of Rh/S$_{12}$−BP catalyst is 0.28 V, implying that the anchored single Rh atom can survive in a matrix of S−doped BP catalyst. In addition, we performed the ab initio molecular dynamics (AIMD) simulations to explain the thermodynamical stability of Rh/S$_{12}$−BP in the water environment. The obtained structure and the time evolutions of energy and temperature were plotted in Figs. S4b and c (Supporting information). The results displayed that the single Rh atom is still stably embedded into the vacancy of S-doped BP substrate after 10 ps without any obvious structural deformation, indicating its good stability in aqueous solutions at ambient temperature. Overall, based on the computed surface Pourbaix diagram, dissolution potential, and AIMD simulations, we predicted that our designed catalysts exhibit enhanced stability under the atmosphere of water and oxygen environments than the instable pristine BP nanosheet [69,70], which may form a class of robust electrocatalysts for various energy applications.

In summary, by means of comprehensive DFT calculations, we explored the catalytic performance of several transition metals anchored on various S-doped BP substrates as the promising catalysts for overall water splitting reactions. The calculation results demonstrated that the anchored TM atoms exhibit interesting spin moments, endowing them different binding strength with oxygenated species, in which the anchored Rh and Pd atoms on S_{12}-BP substrate were suggested as excellent OER catalysts due to their moderate spin densities. More interestingly, Rh/S_{12}-BP also shows superior HER catalytic performance with the ΔG_{H^*} of 0.02 eV, and the P_1 site around Rh atom performs as the active site. Remarkably, this catalyst exhibits high electrochemical and thermodynamical stabilities in aqueous solutions. Therefore, the low overpotential and the high stability render Rh/S_{12}-doped BP a very compelling bifunctional catalyst for overall water splitting, which may pave a new way for advancing sustainable H_2 production.

Declaration of competing interest

The authors declare that they have no known competing financial interests or personal relationships that could have appeared to influence the work reported in this paper.

Acknowledgment

This work was financially supported by the Natural Science Funds (NSF) for Distinguished Young Scholar of Heilongjiang Province (No. JC2018004).

References

[1] S. Geng, F. Tian, M. Li, et al., Nano Res. 15 (2021) 1809–1816.
[2] C.X. Zhao, B.Q. Li, J.N. Liu, J.Q. Huang, Q. Zhang, Chin. Chem. Lett. 30 (2019) 911–914.
[3] T. Cui, Y.P. Wang, T. Ye, et al., Angew. Chem. Int. Ed. 61 (2022) e202115219.
[4] C.Z. He, Y.X. Zhang, J. Wang, L. Fu, Rare Metals 41 (2022) 3456–3465.
[5] Y. Luo, Z. Zhang, M. Chhowalla, B. Liu, Adv. Mater. 34 (2022) e2108133.
[6] H. Zhang, Q. Jiang, J.H.L. Hadden, F. Xie, D.J. Riley, Adv. Funct. Mater. 31 (2020) 2008989.
[7] X. Wan, H. Niu, Y. Yin, et al., Catal. Sci. Technol. 10 (2020) 8339–8346.
[8] J. Wang, M. Zhang, G. Yang, et al., Adv. Funct. Mater. 31 (2021) 2101532.
[9] Y. Wang, G. Qian, Q. Xu, et al., Appl. Catal. B: Environ. 286 (2021) 119881.
[10] B. Zhang, Y. Zheng, T. Ma, et al., Adv. Mater. 33 (2021) e2006042.
[11] L. Chen, Y. Wang, X. Zhao, et al., J. Mater. Sci. Technol. 110 (2022) 128–135.
[12] S. Lu, H.L. Huynh, F. Lou, K. Guo, Z. Yu, Nanoscale 13 (2021) 12885–12895.
[13] C. Walter, P.W. Menezes, M. Driess, Chem. Sci. 12 (2021) 8603–8631.
[14] G. Fu, Y. Wang, Y. Tang, et al., ACS Mater. Lett. 1 (2019) 123–131.
[15] J. Zhang, Q. Zhang, X. Feng, Adv. Mater. 31 (2019) e1808167.
[16] Q. Wang, Q. Feng, Y. Lei, Nat. Commun. 13 (2022) 3689.
[17] Q. Li, Y. Wang, J. Zeng, et al., Chin. Chem. Lett. 32 (2021) 3355–3358.
[18] B. Deng, J. Liang, L. Yue, et al., Chin. Chem. Lett. 33 (2022) 890–892.
[19] S.H. Talib, Z. Lu, X. Yu, et al., ACS Catal. 11 (2021) 8929–8941.
[20] C.C. Cheng, Y.X. Yeh, Y.C. Ting, et al., J. Mater. Chem. A 10 (2022) 8784–8797.
[21] Y. Wang, W. Tian, J. Wan, G. Xiong, et al., Phys. Chem. Chem. Phys. 24 (2022) 10325–10333.
[22] R. Gusmão, M. Veselý, Z. Sofer, ACS Catal. 10 (2020) 9634–9648.
[23] X. Zhai, L. Li, X. Liu, et al., Nanoscale 12 (2020) 10035–10043.
[24] F. Ullah, K. Ayub, T. Mahmood, Int. J. Hydrog. Energy 46 (2021) 37814–37823.
[25] J. Xu, H. Li, Y. Li, et al., Mater. Lett. 303 (2021) 130422.
[26] J.D. Liu, Z.X. Wei, Y.H. Dou, Y.Z. Feng, J.M. Ma, Rare Metals 39 (2020) 874–880.
[27] F. Shi, K. Huang, S. Feng, ChemCatChem 12 (2020) 1913–1921.
[28] J. Hao, Z. Wang, Y. Wang, Phys. Status Solidi. 256 (2019) 1800418.
[29] X. Ren, J. Zhou, X. Qi, et al., Adv. Energy Mater. 7 (2017) 1700396.
[30] L. Zhang, L.X. Ding, G.F. Chen, X. Yang, H. Wang, Angew. Chem. Int. Ed. 58 (2019) 2612–2616.
[31] Y. Chang, A. Nie, S. Yuan, et al., Nanotechnology 30 (2019) 035701.
[32] B. Yang, B. Wan, Q. Zhou, et al., Adv. Mater. 28 (2016) 9408–9415.
[33] X.P. Li, C. Huang, W.K. Han, T. Ouyang, Z.Q. Liu, Chin. Chem. Lett. 32 (2021) 2597–2616.
[34] X.X. Xue, S. Shen, X. Jiang, et al., J. Phys. Chem. Lett. 10 (2019) 3440–3446.
[35] J. Wu, J.H. Li, Y.X. Yu, ACS Appl. Mater. Interfaces 13 (2021) 10026–10036.
[36] L.D. He, P.C. Lian, Y.Z. Zhu, J.P. Zhao, Y. Mei, Chin. J. Chem. 39 (2021) 690–700.
[37] W. Lv, B. Yang, B. Wang, et al., ACS Appl. Mater. Interfaces 10 (2018) 9663–9668.
[38] G. Xu, H. Li, A.S.R. Bati, et al., J. Mater. Chem. A 8 (2020) 15875–15883.
[39] Y. Li, W. Pei, J. He, et al., ACS Catal. 9 (2019) 10870–10875.
[40] H. Qiao, H. Liu, Z. Huang, et al., Adv. Energy Mater. 10 (2020) 2002424.
[41] F. Shi, Z. Geng, K. Huang, et al., Adv. Sci. 5 (2018) 1800575.
[42] G. Kresse, J. Furthmuller, Phys. Rev. B: Condens. Matter. 54 (1996) 11169–11186.
[43] G. Kresse, D. Joubert, Phys. Rev. B 59 (1999) 1758–1775.
[44] P.E. Blochl, Phys. Rev. B Condens. Matter. 50 (1994) 17953–17979.
[45] K. Xiong, B.W. Wang, Z.P. Sun, et al., Rare Metals 41 (2021) 1002–1014.
[46] J.R. Huo, J. Wang, H.Y. Yang, C.Z. He, J. Mol. Model. 27 (2021) 38.
[47] M.C. Groenenboom, R.M. Anderson, J.A. Wollmershauser, et al., J. Phys. Chem. C 124 (2020) 15171–15179.
[48] H. Zhang, G. Liu, L. Shi, J. Ye, Adv. Energy Mater. 8 (2018) 1701343.
[49] Y. Chen, S. Ji, C. Chen, et al., Joule 2 (2018) 1242–1264.
[50] H. Zeng, X. Liu, F. Chen, et al., ACS Appl. Mater. Interfaces 12 (2020) 52549–52559.
[51] Z.X. Wei, Y.T. Zhu, J.Y. Liu, et al., Rare Metals 40 (2021) 767–789.
[52] Y. Qiu, X. Peng, F. Lu, et al., Chem. Asian. J. 14 (2019) 2770–2779.
[53] Y. Wang, E. Song, W. Qiu, et al., Prog. Mater. Sci. Mater. 29 (2019) 256–264.
[54] Z. Li, X. Zhang, X. Zhao, et al., Adv. Mater. 32 (2020) e1907645.
[55] M. Qin, X. Meng, W. Wang, Chem. Phys. Lett. 765 (2021) 138321.
[56] Y. Yang, J. Liu, F. Liu, Z. Wang, D. Wu, J. Mater. Chem. A 9 (2021) 2438–2447.
[57] Z. Xue, X. Zhang, J. Qin, R. Liu, J. Mater. Chem. A 7 (2019) 23091–23097.
[58] Y. Chen, X. Zhang, J. Qin, R. Liu, Mol. Catal. 516 (2021) 111955.
[59] A. Chen, S.V. Nair, B. Miljkovic, H.E. Ruda, Z. Ji, J. Electroanal. Chem. 855 (2019) 113499.
[60] A. Curutchet, P. Colinet, C. Michel, S.N. Steinmann, T.Le Bahers, Phys. Chem. Chem. Phys. 22 (2020) 7031–7038.
[61] B. Zhang, X. Fu, L. Song, X. Wu, Carbon 172 (2021) 122–131.
[62] T. Bo, Y. Liu, J. Yuan, P. Wu, W. Zhou, Comput. Mater. Sci. 185 (2020) 109966.
[63] Z. Liang, X. Zhong, T. Li, M. Chen, G. Feng, ChemElectroChem 6 (2019) 260–267.
[64] J. Wu, Y.X. Yu, J. Colloid. Interface Sci. 623 (2022) 432–444.
[65] S. Wang, D. Jiao, J. Liu, Y. Shang, J. Zhao, New J. Chem. 45 (2021) 8101–8108.
[66] Y. Zhou, G. Gao, Y. Li, W. Chu, L.W. Wang, Phys. Chem. Chem. Phys. 21 (2019) 3024–3032.
[67] G. Xiao, R. Lu, J. Liu, et al., Nano Res. 15 (2021) 3073–3081.
[68] X. Guo, J. Gu, S. Lin, et al., J. Am. Chem. Soc. 142 (2020) 5709–5721.
[69] Y. Wang, B. Yang, B. Wan, et al., 2D Mater. 3 (2016) 035025.
[70] J.O. Island, G.A. Steele, H.S.J.v.d. Zant, A. Castellanos-Gomez, 2D Mater. 2 (2015) 011002.